Theory of Hydro-Equivalent Ignition for Inertial Fusion and Its Applications to OMEGA and the National Ignition Facility

Introduction

In inertial confinement fusion (ICF),[1] a spherical capsule is illuminated either directly with laser light[2] or indirectly within x rays generated by laser irradiation of the walls of a container (hohlraum) enclosing the capsule.[3] The capsule consists of a cryogenic layer of deuterium and tritium (DT) frozen onto the inner surface of a spherical shell of ablator material. Photons are absorbed in the coronal plasma surrounding the shell via inverse bremsstrahlung, and the energy is thermally conducted to the surface of the shell, causing it to ablate. The ablating mass creates an equal and opposite force that causes the remaining shell material to implode. This mechanism is typically known as the "rocket effect." The imploding shell attains a peak implosion velocity before converting a fraction of its kinetic energy into internal energy upon stagnation. The compressed core of an ICF capsule consists of a low-density (tens of g/cm^3) and high-temperature (several keV's) DT plasma (the hot spot) surrounded by a dense (hundreds of g/cm^3) and cold (hundreds of eV's) DT shell. If the thermal energy and areal density of the hot spot are large enough, the alpha particles generated from fusion reactions deposit their energy within the hot spot, triggering a thermal runaway process called "thermonuclear ignition." A robust ignition would launch an alpha-driven burn wave in the surrounding dense fuel, leading to a significant fusion-energy output. The resulting energy gain (target gain = fusion energy/laser energy on target) depends on the shell's areal density (ρR), which determines the fraction of fuel burned (Φ) according to the expression $\Phi = \rho R_{g/cm^2} / \left(7 + \rho R_{g/cm^2}\right)$ (Ref. 4). The shell's areal density is a critical parameter for the onset of ignition since it provides the inertial confinement for the hot-spot pressure.

To date, no significant fusion gain has been achieved in a laboratory setting, although experiments at the National Ignition Facility (NIF) have achieved core conditions, where the fusion energy released exceeds the energy in the fuel and the alpha-particle heating approximately doubles the number of fusion reactions.[5] The Lawson criterion is the metric used to determine how close these implosions are to ignition.[6] This criterion is obtained by balancing the energy lost from the plasma to the total energy gained via fusion reactions, thereby determining the minimum values of performance metrics required to sustain a burning plasma. The Lawson criterion has long been used in magnetic confinement[7] and only more recently has it been applied to ICF implosions in a useful form that depends on experimentally measured quantities.[8–10] The criterion can be expressed through an overall ignition parameter $\chi \equiv P\tau/P\tau_{ig}$, where P is the hot-spot pressure, τ is the hot-spot energy's confinement time, $P\tau_{ig} = 24\, \varepsilon_\alpha T^2 / \langle \sigma v \rangle$ is a function of ion temperature only with $\langle \sigma v \rangle$ representing the fusion reactivity $\left[\langle \sigma v \rangle(T)\right]$, and $\varepsilon_\alpha = 3.5$ MeV is the alpha-particle birth energy. The ignition condition is defined such that when $\chi = 1$, the target gain = 1. Other performance metrics such as the ignition threshold factor (ITF and ITFx)[11] or the minimum energy required for ignition[12,13] can be easily related to the Lawson criterion.[10] The generalized Lawson criterion for ICF was first derived in one dimension by Zhou and Betti[10] and later generalized to three dimensions by Chang *et al.*[9] and Betti *et al.*[8] Throughout the remainder of this article, we will consider only the generalized Lawson criterion.

The 1.8-MJ NIF Laser System is unique in its ability to field ignition-scale indirect- and direct-drive implosions. Because of high costs and low shot-repetition rates, most of the fundamental physics must be investigated at smaller-scale laser facilities such as the Omega Laser Facility.[14] Experiments on the 30-kJ OMEGA laser are not expected to achieve ignition since the amount of laser energy that couples to the target is not enough to achieve the performance metrics required by the Lawson criterion. This gap in laser energy can be bridged using the theory of hydrodynamic equivalence. Hydro-equivalent implosions share a set of performance metrics that enable one to compare two implosions scaled in laser energy. Because the performance metrics scale hydro-equivalently, the Lawson criterion can be scaled up in energy from OMEGA to the NIF. The core idea of this work is to determine the performance required on an OMEGA-scale implosion to predict the achievement of ignition on a hydro-equivalently scaled NIF-sized target. The extrapolation on which this work is based is from the OMEGA Laser

System to a symmetric direct-drive NIF Laser System with two-dimensional (2-D) smoothing by spectral dispersion (SSD).[15] It is important to emphasize that the NIF is currently not configured for symmetric illumination but could be with significant resource investment. This extrapolation will provide both guidance and a goal for OMEGA-scale cryogenic experiments.

The remaining four sections of this article (1) develop the theory of hydrodynamic equivalence in both one and three dimensions, establish design criteria for hydro-equivalent targets, and discuss the limitations of the theory; (2) present hydro-equivalent designs for the NIF and OMEGA laser-energy scales and confirm the theory developed in the previous section; (3) discuss the Lawson criterion parameter and its hydro-equivalent scaling, develop an analytical derivation of the scaling between hydro-equivalent implosions, present 2-D computational simulations supporting this simple model, and draw conclusions from the results; and (4) summarize the implications of this article.

Theory of Hydrodynamic Equivalence

In this section the theory of hydrodynamic equivalence is developed, showing how it connects to existing scaling relations and describing some of its limitations. As previously stated, hydrodynamic equivalence provides a tool for comparing the performance of implosions driven with different energies. The subsections (1) define hydro-equivalency in one dimension; (2) show that one-dimensional (1-D) hydro-equivalent implosions conserve their equivalency in three dimensions; (3) establish design criteria for hydro-equivalent targets; and (4) discuss the limitations of the theory.

1. One-Dimensional Hydrodynamic Equivalence

The simplest model for a 1-D implosion of a thin shell ($\Delta \ll R$) driven by an applied pressure P_{abl} includes the evolution equation for the shell radius R and the shell thickness Δ:

$$M_{sh}\ddot{R} = -4\pi P_{abl}R^2, \qquad (1)$$

$$\Delta = \frac{5M_{sh}}{8\pi\rho_{abl}R^2}, \qquad (2)$$

where ρ_{abl} is the density at the ablation surface. This simple model neglects the fraction of ablated mass and assumes that the shell mass is constant. Equation (1) is Newton's law applied to a thin shell driven by a constant pressure P_{abl}; Eq. (2) shows that the shell expands like $1/R^2$ to conserve mass since the applied pressure maintains a fixed density profile given by $dP/dr = -\rho\ddot{R}$ and $P \sim \rho^{5/3}$ for an isentropic implosion. The

resulting density profile is $\rho = \rho_{abl}(1-x/\Delta)^{3/2}$, where Δ is given by Eq. (2) and $x \equiv R_{abl}-r$ with R_{abl} being the radial location of the shell's outer surface. Equations (1) and (2) can be solved using the initial conditions for R and Δ. We define the initial time of the acceleration phase ($t = 0$) as the time soon after the main shock breaks out of the inner shell surface after the shell is set in motion by the initial shock (or shocks merging near the inner shell surface). For a strong shock, the post-shock velocity of the shell is approximately $V_{ps} \approx \xi_0 C_s(0)$, where $C_s(0)$ is the shell's sound speed after the shocks have passed through the shell. The factor $\xi_0 \equiv (3/\sqrt{5})(P_{sh}/P_{abl})^{1/5}$ is of the order of unity and depends on the ratio of the pressure used to drive the initial shock P_{sh} and the peak ablation pressure P_{abl} used to implode the target. The initial conditions for Eqs. (1) and (2) are

$$R(0) = R_0, \qquad (3)$$

$$\dot{R}(0) = -\xi_0 C_s(0). \qquad (4)$$

By multiplying Eq. (1) by $\dot{R}$ and integrating between $t = 0$ and the end of the acceleration phase when the velocity has reached its maximum value V_{imp} and the radius has shrunk by the convergence ratio $CR_a \equiv R(0)/R_a$, where R_a is the radius at the end of the acceleration phase (note CR_a is the convergence ratio at the end of the acceleration phase and not the total convergence ratio at stagnation), the following energy relation is obtained:

$$\frac{1}{2}M_{sh}V_{imp}^2\left(1 - \frac{\xi_0^2}{M_*^2}\right) = \frac{4\pi}{3}P_{abl}R_0^3\left(1 - \frac{1}{CR_a^3}\right), \qquad (5)$$

where $M_* = V_{imp}/C_s(0)$ is the implosion Mach number. Substituting the mass of a thin shell $M_{sh} = 4\pi\langle\rho\rangle\Delta R^2$ (with $\langle\rho\rangle = 2\rho_{abl}/5$) into Eq. (5) yields the relation between the in-flight aspect ratio (IFAR) and the Mach number M:

$$IFAR \equiv \frac{R(0)}{\Delta(0)} = M_*^2\frac{1 - \xi_0^2/M_*^2}{1 - 1/CR_a^3}. \qquad (6)$$

In the limit of large Mach numbers and large values of CR_a^3, Eq. (6) reduces to the well-known scaling relation $IFAR \approx M_*^2$ (Ref. 16). The implosion model in Eqs. (1) and (2) and their initial conditions can be rewritten using the dimensionless variables $\hat{R} = R/R(0)$, $\hat{t} = tV_{imp}/R(0)$, and $\hat{\Delta} = \Delta/\Delta(0)$:

$$\ddot{\hat{R}} \approx -\frac{3}{2}\frac{1 - \xi_0^2/M_*^2}{1 - 1/CR_a^3}\hat{R}^2, \qquad (7)$$

$$\hat{\Delta} = \frac{1}{\hat{R}^2}, \tag{8}$$

$$\hat{R}(0) = 1, \quad \dot{\hat{R}}(0) = -\frac{\xi_0}{M_*}, \quad \hat{\Delta}(0) = 1. \tag{9}$$

Equations (3)–(6) show that implosions with the same M_*, ξ_0, and CR_a exhibit the same dimensionless trajectories and the same IFAR; therefore, this family of implosions is labeled "hydrodynamically equivalent." By neglecting the term $1/CR_a^3$ in Eqs. (7)–(9), the dimensionless trajectory of a thin shell is uniquely determined by the Mach number M_*. Interestingly, in the limit of large Mach numbers and large convergence ratios, the dimensionless trajectories of both the radius and thickness approach a universal curve. Note that the thin-shell Eqs. (7)–(9) are valid only for large values of M_* and IFAR and as long as the shell's time-dependent aspect ratio R/Δ is of the order of M_*^2. Since R/Δ decreases like R^3, it will eventually become smaller and of the order of M_* (instead of M_*^2). At this point, Eqs. (7)–(9) are no longer valid and the shell thickness will stop increasing; the shell density will start increasing, while the shell pressure will exceed the applied pressure. This limit is considered by Basko:[17] the resulting final pressure at stagnation is proportional to the applied pressure amplified by a power law of the Mach number. According to Basko, that power law is $P_{stag} = P_{abl}M_*^4$, but according to the self-similar solution of Kemp et al.,[13] $P_{stag} = P_{abl}M_*^3$. The important point is that by fixing the Mach number M_* and the applied pressure P_{abl}, all hydro-equivalent thin-shell implosions lead to the same final stagnation pressure.

In laser-driven implosions, a significant portion of the shell mass is ablated by the laser. The model [Eqs. (1) and (2)] of laser-driven implosions must be modified to include the effect of mass ablation. In the presence of mass ablation, the equations of motion are well described by the rocket model:[18]

$$M_{sh}\ddot{R} = V_{ex}\dot{M}_{sh}, \tag{10}$$

$$\dot{M}_{sh} = -4\pi\dot{m}_{abl}R^2, \tag{11}$$

where $\dot{m}_{abl}$ is the mass ablation rate and V_{ex} is the exhaust velocity. Since the exhaust velocity is approximately the sound speed at the critical surface and proportional to a power of the laser intensity or radiation temperature, for a fixed laser intensity, Eq. (10) leads to the well-known rocket equation for the shell velocity,

$$\dot{R} = -\xi_0 C_s(0) - V_{ex}\ln\frac{M_{sh}(0)}{M_{sh}}. \tag{12}$$

Equations (11) and (12) can be rewritten in dimensionless form using the same variables used in Eqs. (7)–(9), leading to

$$\dot{\hat{R}} = -\frac{\xi_0}{M_*} - \frac{V_{ex}}{V_{imp}}\ln\frac{1}{\hat{M}_{sh}}, \tag{13}$$

$$\dot{\hat{M}}_{sh} = -\Psi\hat{R}^2, \tag{14}$$

where $\hat{M}_{sh} = M_{sh}/M_{sh}(0)$ is the dimensionless shell mass and

$$\Psi = \frac{4\pi\dot{m}_{abl}R(0)^3}{M_{sh}(0)V_{imp}}. \tag{15}$$

Since $\dot{m}_{abl}V_{ex}$ is the ablation pressure, the dimensionless parameter Ψ can be rewritten as

$$\Psi = \frac{3}{2}\frac{IFAR}{M_*^2}\frac{V_{imp}}{V_{ex}}. \tag{16}$$

If we consider a family of implosions with the same final fraction of unablated mass (same $\hat{M}_{sh}^f$), the final implosion velocity is given by Eq. (12):

$$V_{imp} = \xi_0 C_s(0) + V_{ex}\ln\left(\frac{1}{\hat{M}_{sh}^f}\right). \tag{17}$$

Notice that for this family of implosions,

$$\frac{V_{ex}}{V_{imp}} = \left(1 - \frac{\xi_0}{M_*}\right)\Bigg/\ln\frac{1}{\hat{M}_{sh}^f} \tag{18}$$

and the remaining mass fraction $\hat{M}_{sh}^f$ depends on the Mach number M_*, the parameter ξ_0, and the ratio V_{ex}/V_{imp}. In the limit of large Mach numbers, the remaining mass fraction depends only on V_{ex}/V_{imp}. After substituting Eq. (18) into Eq. (16),

$$\Psi = \frac{3}{2}\frac{IFAR}{M_*^2}\ln\left(\frac{1}{\hat{M}_{sh}^f}\right)\Bigg/\left(1 - \frac{\xi_0}{M*}\right). \tag{19}$$

To achieve the same dimensionless trajectory and the same unablated mass fraction, Eqs. (13) and (14) require the same values of M_*, ξ_0, and Ψ. An explicit relation between $\hat{M}_{sh}$ and $\hat{R}$ can be derived by integrating Eq. (13) after multiplying by Eq. (14):

$$\frac{\Psi}{3}(\hat{R}^3 - 1) = \frac{\xi_0}{M_*}(\hat{M}_{sh} - 1)$$

$$-\left(1 - \frac{\xi_0}{M_*}\right)\frac{\hat{M}_{sh} - 1 - \hat{M}_{sh}\ln\hat{M}_{sh}}{\ln\hat{M}_{sh}^f}. \tag{20}$$

Rewriting Eq. (20) at the end of the acceleration phase yields a simple relation for the parameter Ψ:

$$\Psi = \left\{\frac{1 - \hat{M}_{sh}^f}{\ln\left(1/\hat{M}_{sh}^f\right)} - \hat{M}_{sh}^f + \frac{\xi_0}{M_*}\left[1 - \frac{1 - \hat{M}_{sh}^f}{\ln\left(1/\hat{M}_{sh}^f\right)}\right]\right\}$$

$$\times \frac{3}{1 - CR_a^{-3}}, \tag{21}$$

indicating that for large Mach numbers and convergence ratios, the parameter Ψ depends only on the final fraction of unablated mass. Substituting Eq. (20) for Ψ leads to a relation between the IFAR and the Mach number,

$$IFAR = M_*^2 \frac{1 - \xi_0/M_*}{1 - 1/CR_a^3} \Theta, \tag{22}$$

$$\Theta = \frac{2}{\ln\hat{M}_{sh}^f}\left[\frac{1 - \hat{M}_{sh}^f}{\ln\hat{M}_{sh}^f} + \hat{M}_{sh}^f - \frac{\xi_0}{M_*}\left(1 + \frac{1 - \hat{M}_{sh}^f}{\ln\hat{M}_{sh}^f}\right)\right]. \tag{23}$$

In the limit of large M_*, the factor Θ depends only on the remaining mass fraction. In the limit of $1 - \hat{M}_{sh}^f \ll 1$, $\Theta \to \left(1 + \xi_0/M_*\right)$ and Eq. (21) reproduces Eq. (6) for the "no-ablation" case. For arbitrary $\hat{M}_{sh}^f < 1$, the rocket model maintains the $IFAR \sim M_*^2$ scaling of the no-ablation case, but the proportionality factor depends mostly on the unablated mass fraction. To preserve hydro-equivalence in the presence of ablation, one must preserve the value of $\hat{M}_{sh}^f$, thereby requiring that V_{ex}/V_{imp} be constant. Within the framework of the rocket model, hydro-equivalence requires constant values for M_*, V_{ex}/V_{imp}, ξ_0, and CR_a. Targets with these same dimensionless parameters exhibit the same dimensionless trajectory, IFAR, and unablated mass fraction.

It is useful to consider the ablation velocity V_{abl}, defined as the penetration velocity of the ablation front into the imploding shell. The ablation velocity is given by the ratio

$$V_{abl} = \frac{\dot{m}_{abl}}{\rho_{abl}}. \tag{24}$$

Equation (24) can be normalized to the implosion velocity and rewritten as

$$\frac{V_{abl}}{V_{imp}} = \frac{3}{5}\frac{1}{M_*^2}\frac{V_{imp}}{V_{ex}}, \tag{25}$$

where the relation $P_{abl} \approx \dot{m}_{abl}V_{ex}$ has been used. This shows that the ratio V_{imp}/V_{ex} depends on the Mach number and the ratio V_{abl}/V_{imp}. Therefore, the requirements for 1-D hydro-equivalency can also be satisfied by fixing the values of M_*, V_{abl}/V_{imp}, ξ_0, and CR_a.

For optimized implosions, the value of the convergence ratio at the end of the acceleration phase is not an arbitrary quantity. Typically the shell is driven inward until the remaining implosion time is of the same order of the sound speed's traveling time through the shell:

$$\frac{R_a}{V_{imp}} \sim \frac{\Delta_a}{C_{sa}}, \tag{26}$$

where the subscript "a" indicates the end of the acceleration phase. This condition implies that for $R < R_a$, the shell density and pressure increase, with the latter exceeding the applied pressure. Therefore, even if the laser is still on for $R < R_a$, the effects on the implosion dynamics are negligible since the shell pressure exceeds the applied pressure. For a constant ablation pressure $C_{sa} = C_s(0)$, Eq. (26) requires that the IFAR at the end of the acceleration phase scales as the Mach number (rather than M_*^2): $IFAR_a = \nu M_*$, where ν is a constant of proportionality. Since the unablated mass fraction can be written as $\hat{M}_{sh}^f = \hat{\Delta}_a/CR_a^2$, $IFAR_a = IFAR/\left(CR_a^3\hat{M}_{sh}^f\right)$, leading to an end-of-acceleration convergence ratio

$$CR_a = \left(\frac{M_*}{\nu}\frac{1 - \xi_0/M_*}{1 - 1/CR_a^3}\frac{\Theta}{M_{sh}^f}\right)^{1/3} \approx \left(\frac{M_*}{\nu}\frac{\Theta}{M_{sh}^f}\right)^{1/3}, \tag{27}$$

where the last term on the right-hand side is obtained in the large M_* limit.

In summary, 1-D hydro-equivalence is obtained for fixed values of M_*, V_a/V_{imp}, and ξ_0. Implosions with equal values of these three dimensionless parameters exhibit the same unablated mass fraction, the same IFAR (both initial IFAR and

at the end of the acceleration phase), the same dimensionless trajectory, and the same dimensionless thickness. Given the importance of the stagnation pressure to the ignition conditions, we consider hydro-equivalent implosions driven by the same ablation pressures P_{abl}, achieving the same final stagnation pressure $P_{stag} \sim P_{abl} M_*^3$.

The last step is to translate the hydro-equivalence requirements into constraints on the physical parameters. Using the isentropic relation $P \sim \alpha \rho^{5/3}$ (where α is the adiabat), the Mach number and the ratio V_{abl}/V_{imp} can be rewritten as

$$M_*^2 \sim \frac{V_{imp}^2}{\alpha^{3/5} P_{abl}^{2/5}}, \quad \frac{V_{abl}}{V_{imp}} \sim \frac{\dot{m}_{abl} \alpha^{3/5}}{P_{abl}^{3/5} V_{imp}}. \quad (28)$$

Since both the ablation pressure and ablation rate depend on the laser intensity I_L (for direct drive) or radiation temperature T_{rad} (for indirect drive), Eq. (28) shows that fixing P_{abl} (and $\dot{m}_a$), M_*, and V_{abl}/V_{imp} requires setting the values of implosion velocity V_{imp}, adiabat α, and laser intensity I_L (or radiation temperature T_{rad}). Once the ablation pressure and shell adiabat are set, the parameter ξ_0 is not an independent parameter since the shock pressure P_{sh} is directly proportional to the adiabat $P_{sh} \sim \alpha \rho_{ps}^{5/3}$, where the post-shock density ρ_{ps} is roughly $4\times$ the initial density for a strong shock. It follows that all hydro-equivalent implosions designed to achieve the same stagnation pressure in one dimension require equal values of the implosion velocity, shell adiabat, and laser intensity (for direct drive) or radiation temperature (for indirect drive).

2. Three-Dimensional Hydrodynamic Equivalence

In this subsection, we show that the requirements for 1-D hydro-equivalence guarantee equivalence in three dimensions provided that the initial seeds for the hydrodynamic instabilities scale proportionally to the size of the target radius R. The departure from spherical symmetry is caused primarily by the Richtmyer–Meshkov[19,20] (RM) and Rayleigh–Taylor[21,22] (RT) instabilities. Below, we will apply the hydro-equivalence concepts to only the RT instability since the RM instability follows similar arguments.

In ICF implosions, the RT instability develops on the ablation front during the acceleration phase and at the inner shell surface during the deceleration phase. We first consider the acceleration phase. Depending on the initial level of nonuniformities and the unstable spectrum, the RT instability can either be contained within the linear regime or develop a fully nonlinear bubble front. We will consider these two cases separately.

In the linear regime, the RT growth rates approximately follow Takabe's formula.[23,24] The number of e foldings of growth is the integral of the growth rates over the duration of the acceleration phase (t_0), leading to

$$N_e^{RT} = \int_0^{t_0} \gamma_{RT} dt = \int_0^{t_0} \left(\sqrt{kg} - 3k V_{abl} \right) dt, \quad (29)$$

where k is the wave number $k \equiv \ell/R$, ℓ is the mode number, R is the time-dependent shell radius, $g = -\ddot{R}$ is the shell acceleration, and V_{abl} is the ablation velocity. Given that all hydro-equivalent targets have the same dimensionless radius $\hat{R}$ and are driven up to the same convergence ratio CR_a, taking the dimensions out of the expression on the right-hand side of Eq. (29) yields

$$N_e^{RT} = \int_{CR_a^{-1}}^{1} \left(\sqrt{\ell \frac{\ddot{\hat{R}}}{\hat{R}}} - 3\frac{\ell}{\hat{R}} \frac{V_{abl}}{V_{imp}} \right) \frac{d\hat{R}}{\dot{\hat{R}}}, \quad (30)$$

where $\hat{R} = R/R_0$. As discussed in the previous subsection, 1-D hydro-equivalence requires equal values of V_{abl}/V_{imp}; therefore Eq. (30) shows that hydro-equivalent implosions exhibit the same RT growth factors for all mode numbers. The effects of the RT instability on target performance can be assessed by comparing the mode amplitude η_ℓ^a with the target thickness Δ_a at the end of the acceleration phase for each mode. Using the results of the rocket model for the target thickness $\left(\Delta_a = \Delta_0 CR_a^2 \hat{M}_{sh}^f \right)$, the ratio η_ℓ^a/Δ_a can be written as

$$\frac{\eta_\ell^a}{\Delta_a} = \frac{\eta_\ell(0) e^{N_e^{RT}}}{\Delta_0 CR_a^2 \hat{M}_{sh}^f}. \quad (31)$$

Since CR_a and $\hat{M}_{sh}^f$ are the same for hydro-equivalent implosions, Eq. (31) shows that three-dimensional (3-D) hydro-equivalence for the linear RT instability is attained when the initial seeds $\eta_\ell(0)$ are proportional to the initial target thickness.

While Eqs. (30) and (31) prove 3-D equivalence in the linear phase of the RT instability, the most important effects of the RT instability occur when the RT bubble front becomes non-linear and penetrates deeply into the target. It is well known that a fully developed RT bubble front grows proportionally to the distance traveled by the shell during the acceleration phase. By defining the bubble front's penetration distance h_b, the well-known scaling relation $h_b = \beta g t^2$ applies for a fully developed, fully nonlinear multimode bubble front with the coefficient $\beta \approx 0.05$ to 0.07 (Refs. 25–28). For a time-dependent acceleration, the dimensionally correct bubble-front penetration would be $h_b = 2\beta \int_0^t dt' \int_0^{t'} dt'' g(t'')$. At the end of the accel-

eration phase, the parameter h_b can be written in terms of the distance traveled by the shell during the acceleration phase:

$$h_b^a = 2\beta(R_0 - R_a) = 2\beta R_0(1 - CR_a^{-1}). \qquad (32)$$

The figure of merit that measures the effects of the RT instability on the target performance is the ratio between the bubble-penetration distance and the shell thickness at the end of the acceleration. Using the results of the rocket model that ratio is

$$\frac{h_b^a}{\Delta_a} = \frac{2\beta}{\hat{M}_{sh}^f} IFAR \frac{(1 - CR_a^{-1})}{CR_a^2}. \qquad (33)$$

Since all 1-D hydro-equivalent implosions exhibit equal values of $\hat{M}_{sh}^f$, IFAR, and CR_a, the nonlinear RT figure of merit h_b^a / Δ_a will be the same for hydro-equivalent implosions. It follows that the effects of the acceleration-phase RT instability on target performance are the same for hydro-equivalent implosions regardless of whether the RT perturbation growth remains within the linear phase or grows into the fully developed nonlinear regime provided that the initial RT seeds scale with the target thickness.

While the acceleration-phase RT instability is fully hydro-equivalent, the deceleration-phase RT instability is not. The growth rate of the deceleration-phase RT has a similar form to Eq. (30) with the exception that the coefficient of the ablative stabilization is 1.4 instead of 3 (Ref. 29) and that mass ablation is driven by the heat leaving the hot spot rather than the heat flux coming from the laser (or x rays). The RT growth rate in the constant deceleration phase on the inside of the shell was fit to the following equation:

$$\gamma_{RT} = 0.9\sqrt{\frac{k\langle g \rangle}{1 + k\langle L_m \rangle}} - 1.4k\langle \overline{v_{abl}} \rangle, \qquad (34)$$

where k is the wave number, $\langle g \rangle$ is the average acceleration, $\langle L_m \rangle$ is the density scale length, and $\langle \overline{v_{abl}} \rangle$ is the deceleration-phase ablation velocity. In this case the deceleration-phase ablation velocity depends on the Spitzer conductivity[30] of the hot spot: $\langle \overline{v_{abl}} \rangle \sim T_0^{5/2} / R_{hs}\rho_{sh}$, where T_0 is the central hot-spot temperature, R_{hs} is the hot-spot radius, and ρ_{sh} is the shell density. It is possible to show that the ablative stabilization term for the deceleration phase is not hydro-equivalent but instead depends on the target size like $\langle \overline{v_{abl}} \rangle \sim R^{-0.5}$. The ablative stabilization of the deceleration-phase RT is important only for implosion velocities exceeding 400 km/s or when the alpha-particle heating is significantly close to ignition conditions, leading to large ablation velocities. Since alpha-particle heating is clearly not hydro-equivalent, as long as hydro-equivalent targets without alpha-particle energy deposition are compared, the effects of the ablative stabilization on the deceleration-phase RT growth can be neglected for $V_{imp} < 400$ km/s and the conditions for hydro-equivalency of the RT instability are retained as well for the deceleration phase. A more-detailed analysis of hydro-equivalency of the deceleration phase is the subject of a forthcoming publication.

In summary, the conditions of 1-D hydro-equivalency (see **One-Dimensional Hydrodynamic Equivalence**, p. 2) requiring equal values of implosion velocity V_{imp}, shell adiabat α, and laser intensity I_L (for direct drive) or radiation temperature T_{rad} (for indirect drive) guarantee 3-D hydrodynamic equivalence provided that the initial level of surface roughness scales proportionally to the target size. If the main source of nonuniformities is laser imprinting (as in the case of direct drive), 3-D hydro-equivalence requires that the relative size of the laser-intensity variations ($\delta I/I$) be the same among hydro-equivalent targets.

3. Design Criteria for Hydro-Equivalent Targets

This section highlights the design criteria for direct-drive hydro-equivalent implosions. To design a family of implosions with the same V_{imp}, α, and I_L, one must specify the target radius and thickness, as well as the laser pulse shape. The latter consists of an initial low-intensity pulse (also called the "foot") that sets the adiabat of the shell through one or more shocks and a main drive that accelerates the shell to the final implosion velocity. While there are different ways of designing the foot of the pulse, the main drive is defined by the total energy E_L, the peak power P_L, and the main pulse length t_L. Most of the pulse energy is contained within the main pulse. The energy, power, and length of the main pulse are related through $E_L \approx P_L t_L$. Since the laser power is $P_L \approx 4\pi R_0^2 I_L$, keeping the same intensity on target requires scaling the laser power, with the target surface $P_L \sim R_0^2$. To drive the capsule to the same final implosion velocity, the pulse length must be proportional to the implosion time $t_L \sim R_0 / V_{imp}$ and, therefore, the laser energy must scale as $E_L \sim 4\pi R_0^3 I_L / V_{imp}$. It follows that for hydro-equivalent implosions, the laser energy must scale as the target volume $E_L \sim R_0^3$. For hydro-equivalent targets, the final shell kinetic energy scaling is proportional to the laser energy in the main drive, leading to $(1/2)M_{sh}V_{imp}^2 \sim E_L$. To achieve the same implosion velocity, the target mass must, therefore,

scale with the laser energy $M_{sh} \sim E_L \sim R_0^3$. Since the target mass is proportional to the shell volume $M_{sh} \sim 4\pi R_0^2 \Delta_0 \rho_0$, for the same initial density, the shell thickness must scale with the target radius $\Delta_0 \propto R_0$.

The basic design criteria for hydro-equivalent implosions consist of specifying the foot of the laser pulse to launch shocks of the same strength to set the shell on the same adiabat α, using a total laser energy proportional to the target volume, $E_L \sim R_0^3$; a peak laser power proportional to the target surface, $P_L \sim R_0^2$;

a pulse length proportional to the target radius, $t_L \sim R_0$; and a shell thickness proportional to the shell radius, $\Delta_0 \propto R_0$. One can express these criteria in terms of laser energy rather than target radius, leading to $R_0 \sim E_L^{1/3}$, $\Delta_0 \sim E_L^{1/3}$, $P_L \sim E_L^{2/3}$, and $t_L \sim E_L^{1/3}$. This scaling can be applied to various performance metrics that have been analytically derived and fit to power laws from simulation databases previously developed.[8,31] Table 137.I reviews most of the important ICF performance metrics and their hydro-equivalent scaling with laser energy.

Table 137.I: Hydrodynamic scaling relations for ICF implosions and their hydro-equivalent scaling relations for 350-nm light. ($I_{15} = I_L / 10^{15}$; T_n is the neutron-averaged ion temperature.)

Performance Metric	Scaling Relation	Hydro-Equivalent Scaling
Hydrodynamic efficiency	$\eta \approx \dfrac{0.051}{I_{15}^{0.25}} \left[\dfrac{V_{imp}(cm/s)}{3 \times 10^7} \right]^{0.75}$	Constant
Neutron yield $(\times 10^{16})$	$Y_{1\text{-}D} \approx \left(\dfrac{T_n}{4.7} \right)^{4.72} \left[\rho R_{tot(n)} \right]^{0.56} \left(\dfrac{m_{sh}^{stag}}{0.12} \right)$	$Y_{1\text{-}D}^{no\,\alpha} \sim E_L^{3/2}$
Shell areal density (g/cm^2)	$(\rho R)_{max} \approx \dfrac{1.2}{\alpha_{inn}^{0.54}} \left[\dfrac{E_L(kJ)}{100} \right]^{0.33} \left[\dfrac{V_{imp}(cm/s)}{3 \times 10^7} \right]^{0.06}$	$(\rho R)_{max} \sim E_L^{3/2}$
Shell density (g/cm^2)	$\langle \rho \rangle_{\rho R} \approx \dfrac{425}{\alpha_{inn}^{1.12}} I_{15}^{0.13} \left[\dfrac{V_{imp}(cm/s)}{3 \times 10^7} \right]$	Constant
Shell IFAR	$IFAR \approx \dfrac{40\, I_{15}^{-0.27}}{\langle \alpha_{if} \rangle^{0.72}} \left[\dfrac{V_{imp}(cm/s)}{3 \times 10^7} \right]^{2.12}$	Constant
Hot-spot areal density (g/cm^2)	$\rho R_{hs} \approx \dfrac{0.31}{\alpha_{inn}^{0.55}} \left[\dfrac{E_L(kJ)}{100} \right]^{0.27} \left[\dfrac{V_{imp}(cm/s)}{3 \times 10^7} \right]^{0.62}$	$\rho R_{hs} \sim E_L^{0.27}$
Hot-spot temperature (keV)	$\langle T_{hs} \rangle \approx \dfrac{2.96}{\alpha_{inn}^{0.15}} \left[\dfrac{E_L(kJ)}{100} \right]^{0.07} \left[\dfrac{V_{imp}(cm/s)}{3 \times 10^7} \right]^{1.25}$	$\langle T_{hs} \rangle \sim E_L^{0.07}$
Hot-spot pressure (Gbar)	$\langle P_{hs} \rangle \approx \dfrac{345}{\alpha_{inn}^{0.90}} \left[\dfrac{V_{imp}(cm/s)}{3 \times 10^7} \right]^{1.85}$	Constant
Stagnation aspect ratio	$A_{stag} \approx \dfrac{1.48}{\alpha_{inn}^{0.19}} \left[\dfrac{V_{imp}(cm/s)}{3 \times 10^7} \right]^{0.96}$	Constant

4. Non-Hydro-Equivalent Physics

Although the hydro-equivalent scaling relations hold well over nearly two orders of magnitude in laser energy (see the next section below), not all of the physical processes that occur in ICF implosions scale hydrodynamically. Hydrodynamic equivalence breaks down when nonscalable physics significantly impact target performance. A nonexhaustive list of nonscalable physics includes radiation transport, thermal conduction, fusion reactions, and laser–plasma interactions (LPI's). Radiation transport can significantly impact radiation and shell-ablation physics in both the acceleration and deceleration phases. If the mean free path of photons is larger than the stopping power of the ablator of an implosion capsule, these photons will penetrate into the DT fuel and deposit their energy, thereby raising the adiabat. This occurs on smaller-scale targets, such as those on OMEGA.

Thermal transport in the hot spot is not hydro-equivalent. As shown by Zhou and Betti,[31] the hot-spot temperature scales weakly with laser energy (or target size): $T_{hs} \sim E_L^{0.07} \sim R^{0.21}$. Since the fusion yield is a strong function of temperature, this weak dependence becomes important when scaling ICF implosions from OMEGA to the NIF. Another non-hydro-equivalent effect is the ablative stabilization of the deceleration-phase RT instability as discussed in the next section.

Fusion-energy deposition and laser scattering caused by LPI's are inherently nonscalable hydrodynamically since alpha-particle energy deposition depends on the shell's areal density relative to a fixed mean-free path as well as on the proximity to the ignition conditions, and the LPI's are threshold-dependent instabilities. This means that all hydrodynamic quantities (except the gain) must be calculated without alpha-particle deposition (no-alpha quantities). Therefore, when scaling up in size and energy to assess the target performance with respect to the ignition conditions, one must use an ignition criterion given in terms of no-alpha quantities.[8,9] LPI's will not be considered in this work. Although a significant amount of work has been invested in understanding LPI effects on direct-drive target performance[32–36] and two-plasmon–decay thresholds,[37–41] this work will assume that if any threshold is exceeded on some energy scale versus another, a mitigation strategy will be employed to address it.

Hydro-Equivalent Implosion Design

In this section we will cover the design and performance of the two hydro-equivalent implosion designs that will be used for the remainder of this article. The latter half of this section will compare the designs to the hydro-equivalent scaling predictions outlined in **Theory of Hydrodynamic Equivalence** (p. 2).

The OMEGA-scale target is based on current cryogenic targets that are routinely imploded on OMEGA.[42] The OMEGA-scale target [shown in Fig. 137.1(a)] has ~10 μm of plastic ablator, 41 μm of DT ice, and an outer radius of 430 μm. This design is imploded with 27 kJ of laser energy, and when simulated with the multidimensional hydrocode *DRACO*,[43] it achieves an implosion velocity of ~350 km/s, has an average in-flight adiabat of 3, and an IFAR$_{R = 2/3R_0}$ of 26. The IFAR is calculated when the shell radius is approximately 2/3 of its initial inner radius. It achieves a neutron-averaged areal density of 300 mg/cm^2 and a neutron yield of 1.6×10^{14} in 1-D simulations. The NIF-scale target [shown in Fig. 137.1(b)] is geometrically scaled from the OMEGA-scale target using the hydro-equivalent scaling relations developed on p. 2. This results in a factor-of-4 increase in the target radius when scaling the laser energy up to 1.84 MJ. Because of differences in radiation transport at these two laser-energy scales, a small change in the target design is required to compensate for deviations from hydro-equivalence. The OMEGA-scale target has insufficient preheat shielding in the CH ablator, which results in an increase in the fuel adiabat when the ablator prematurely ablates. Some of the plastic ablator in the NIF-scale design is mass-equivalently exchanged for DT ice. This leads to lower preheat shielding, resulting in the adiabat remaining the same for the two implosions. The NIF-scale target has the same implosion velocity, adiabat, and IFAR but is predicted to achieve a neutron-averaged areal density of 1.2 g/cm^2 and a 1-D yield of 8.6×10^{16} without alpha-particle deposition. When alpha-particle deposition is turned on, the implosion achieves a neutron yield of 3.3×10^{19}, resulting in a gain of 49.

(a) OMEGA   (b) NIF

TC10868JR
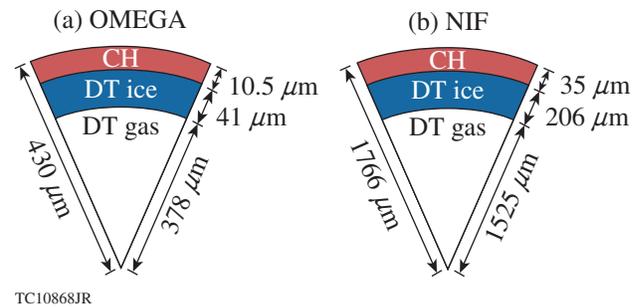
Figure 137:1
Cryogenic target geometry and composition for (a) OMEGA-scale and (b) NIF-scale targets.

When plotted in terms of laser intensity and dimensionless time t/t_{bang}, the laser pulses for the NIF and OMEGA are virtually identical as shown in Fig. 137.2. Here, t_{bang} is the so-called "bang time," defined as the time of peak neutron rate. The time evolution of the implosion velocity and IFAR are the same for NIF-scale and OMEGA-scale targets. Figure 137.3 shows the
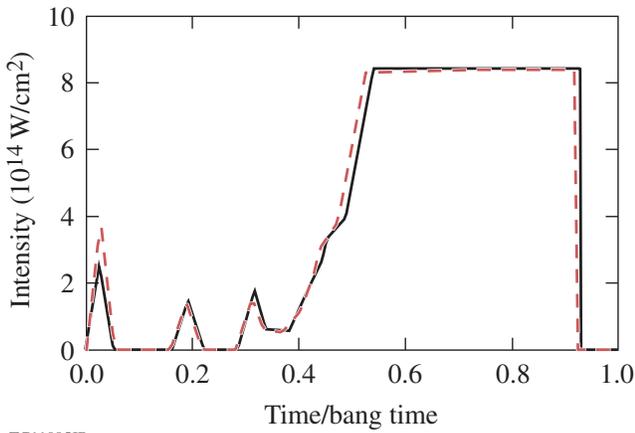
Figure 137.2
Triple-picket laser-intensity pulses versus normalized time (t/t_{bang}) for the NIF-scale (solid black line) and OMEGA-scale (dashed red line) targets.
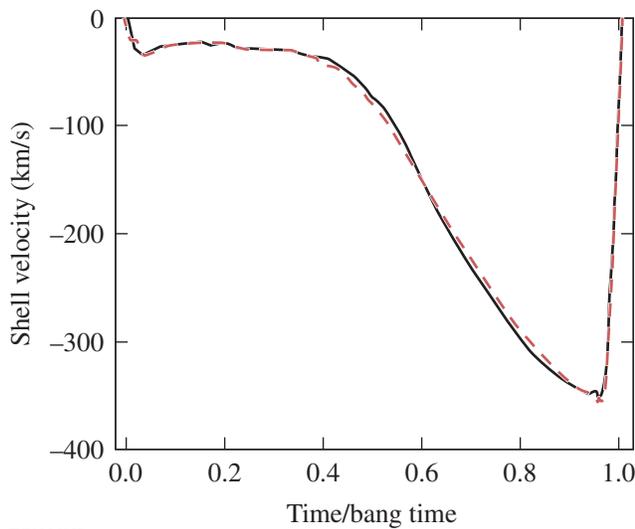
Figure 137.3
Shell velocity versus normalized time for the NIF-scale (solid black line) and OMEGA-scale (dashed red line) targets.

shell velocity versus normalized time for the NIF-scale and OMEGA-scale designs in solid black and dashed red lines, respectively. The two curves are nearly identical, illustrating that they have the same 1-D hydrodynamics. Figure 137.4 plots the IFAR against normalized time and it too shows hydro-equivalent behavior, illustrating that they have the same acceleration-phase RT growth in three dimensions since the adiabats and implosion velocities are the same. Figure 137.5 shows the areal

density versus normalized time for the NIF-scale target (solid black) and the OMEGA-scale target (dashed red) scaled by the energy ratio of the two designs, $\varepsilon \equiv E_L^{NIF} / E_L^{\Omega}$, to the one-third power. This scaling comes from the laws described in **Theory of Hydrodynamic Equivalence** (p. 2) and shows the 1-D
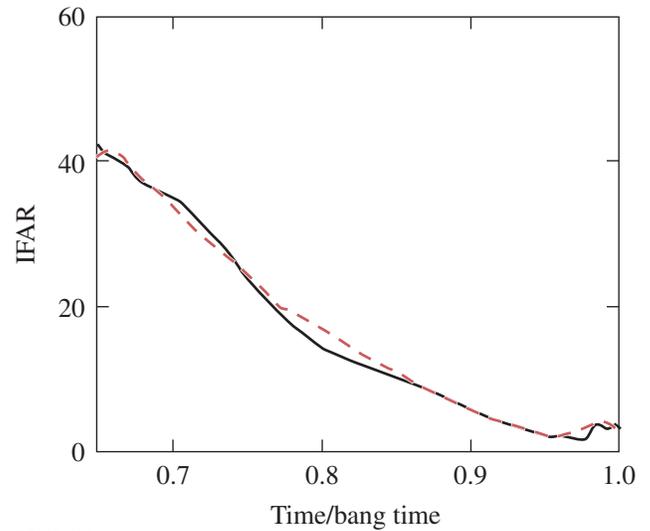
Figure 137.4
In-flight aspect ratio (IFAR) versus normalized time for the NIF-scale (solid black line) and OMEGA-scale (dashed red line) targets.
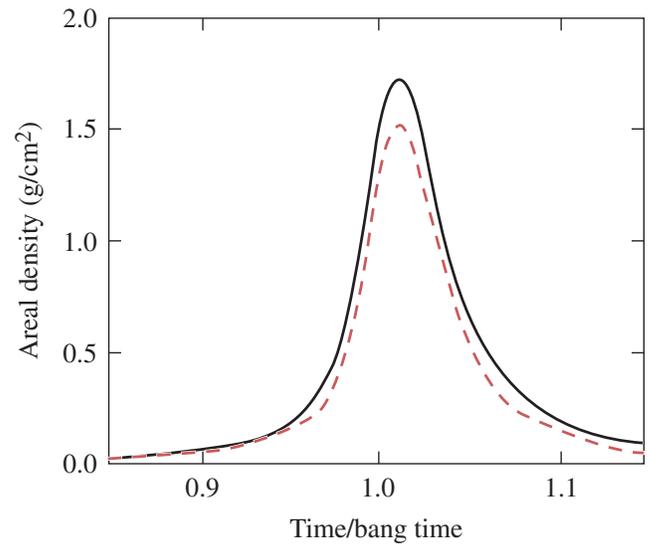
Figure. 137.5
Scaled total areal density versus normalized time for the NIF-scale (solid black line) and OMEGA-scale (dashed red line) targets multiplied by $\varepsilon^{1/3}$.

areal density and neutron rate scale as predicted. Figure 137.6 compares the neutron rate versus normalized time, where the NIF neutron rate is shown as a solid black line and the scaled OMEGA neutron rate as a dashed red line, which scales as $\varepsilon^{7/6}$. The neutron rate scales with $E_L^{7/6}$ because the neutron yield scales as $E_L^{3/2}$ and time scales as $E_L^{1/3}$. This shows good agreement between the theory and simulations.
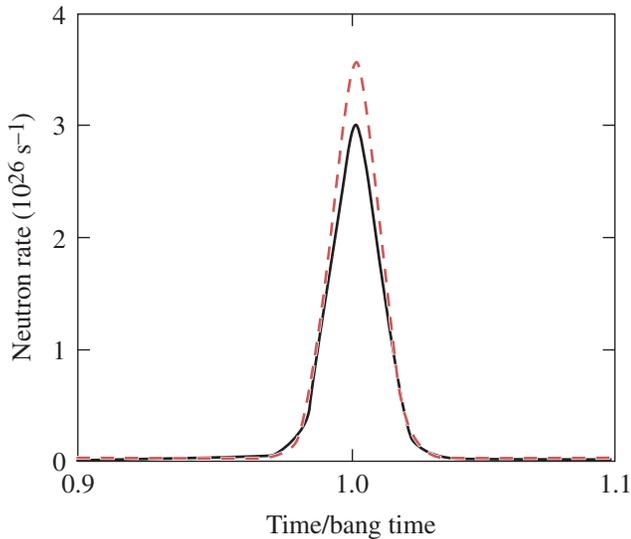
TC10870JR2

Figure 137.6
Scaled total neutron rate versus normalized time for the NIF-scale (solid black line) and OMEGA-scale (dashed red line) targets multiplied by $\varepsilon^{7/6}$.

In terms of multidimensional performance, the two designs are very nearly hydro-equivalent. Two-dimensional *DRACO* simulations were run to assess the performance of the implosions and compare it with the hydro-equivalent scaling theory. All simulations used the *SESAME*[44,45] equation of state for the plastic ablator and FPEOS[46] for the DT fuel. Single-mode simulations were performed in half-wavelength wedges with a minimum of 20 azimuthal cells and sufficient radial zoning to ensure a minimum of six points in the $1/k$ distance away from the ablation surface. The radial zoning was increased with ℓ-mode number to keep the same spatial aspect ratio in the Lagrangian mesh throughout the entire set. This ensured that the amplitudes of the higher harmonics were typically smaller than one tenth of the fundamental-mode amplitude. It is important to note that the seed amplitude between the two designs was kept hydro-equivalent by a factor of $\varepsilon^{1/3}$ in accordance with the change in target size. It should also be mentioned that all of the simulations containing an inner-surface ice roughness had a power spectrum whose amplitude scaled as ℓ^{-2}, where ℓ spanned every even

mode from 2 to 50, unless otherwise specified. These simulations were performed in 90° wedges, and the minimum number of azimuthal cells required to adequately resolve the physical impact of these perturbations was ten per half-wavelength at mode 50.

In the acceleration-phase RT growth, the seed amplitude was set by a single cosine surface perturbation on the outside of the shell such that the growth of the mode was always in the linear stage. Simulations of the single-mode linear growth factor confirm that the acceleration-phase RT growth factors scale approximately hydro-equivalently. Figure 137.7 shows the acceleration-phase linear growth factor versus the ℓ mode for the NIF-scale (solid black) and OMEGA-scale (dashed red) designs. The two curves are close together for ℓ modes ranging from 10 to 300. The small difference between the two curves is attributed to the non-hydro-equivalent radiation transport that increases the scaled density gradient scale length on the OMEGA-scale target with respect to the NIF-scale target. The initial amplitude of the mode is chosen just after the beginning of the acceleration phase, where the effect of any phase inversions resulting from shock breakout have already taken place. Despite these differences, the acceleration-phase growth factors of the two designs are within 20% of each other, justifying the statement of their hydro-equivalence.

A series of single-mode growth factor simulations in the deceleration phase were performed and verified that the deceleration phase is not exactly hydro-equivalent as expected (see **Non-Hydro-Equivalent Physics**, p. 8). In this case the seed perturbation was set as a single cosine-mode density perturbation
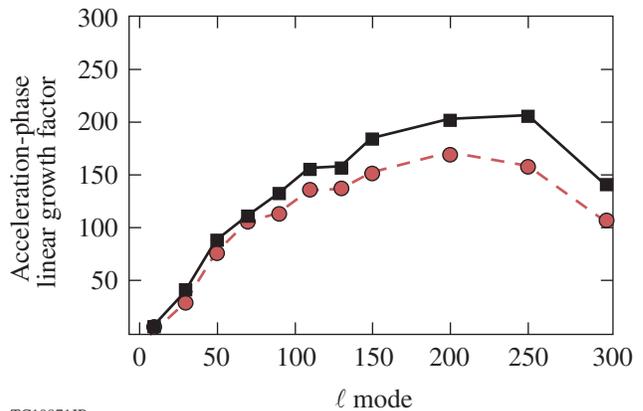
TC10871JR

Figure 137.7
Single-mode linear growth factors versus ℓ mode for acceleration-phase RT growth for the NIF-scale (solid black line) and OMEGA-scale (dashed red line) targets.
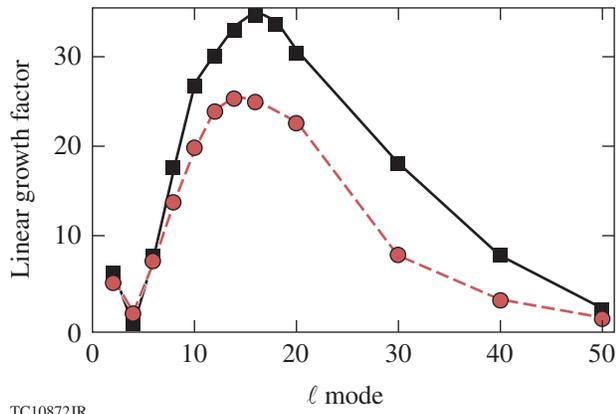
TC10872JR

Figure 137.8
Single-mode linear growth factors versus ℓ mode for deceleration-phase RT growth for the NIF-scale (solid black line) and OMEGA-scale (dashed red line) targets.

on the inside of the target at the DT gas/ice interface. Figure 137.8 shows the total linear growth factor versus ℓ mode for the two designs. It shows that the linear growth factors are comparable for low-ℓ modes but diverge for $\ell > 10$. A phase inversion first occurs at mode $\ell = 4$ (and for every mode greater than 4), giving the illusion that the mode does not grow. The difference between the growth factors of the two designs can be explained by applying the theory developed in Ref. 29, as outlined in **Theory of Hydrodynamic Equivalence** (p. 2). The difference in the linear RT growth factors has little impact on the yield-over-clean (YOC) when performing more-representative simulations, where we define the YOC as the multidimensional yield divided by the 1-D yield. A series of multimode ice spectrum simulations were performed to study their effect on the YOC, where the amplitudes of the modes were not constrained to be within the linear regime. As shown in Fig. 137.9, the YOC decreases at the same rate for both the NIF-scale (solid black line) and OMEGA-scale (dashed red line) targets as a function of the normalized ice roughness. This is the case for both spectrums where the ℓ mode ranged from 2 to 36 (squares) and 10 to 36 (circles). Altering the starting mode in the spectrum made it possible for a different ℓ mode to dominate the hot-spot dynamics to ensure the YOC was the same for any implosion. Choosing an end mode of 36 in this case instead of 50 had no significant effect in the simulations other than decreasing the required computation time.

To summarize, hydro-equivalent designs were presented and tested against the hydro-equivalent theory to ensure hydro-equivalence. In terms of 1-D hydro-equivalence, the designs had identical implosion velocities, laser intensities, adiabats,

and IFAR's. The target geometry scaled with the laser energy, and when applied to the scaling laws shown in Table 137.I, the simulated performance metrics were in good agreement with theory (Figs. 137.3 and 137.4). In terms of multidimensional hydro-equivalence, similar RT growth in the acceleration phase (Fig. 137.7) was predicted by theory and corroborated by simulations. Slight differences in the deceleration phase were predicted by linear theory and seen in simulations (Fig. 137.8); however, this effect is negligible in terms of performance for these two designs (as shown in Fig. 137.9). The OMEGA-scale and NIF-scale designs presented are approximately hydro-equivalent.
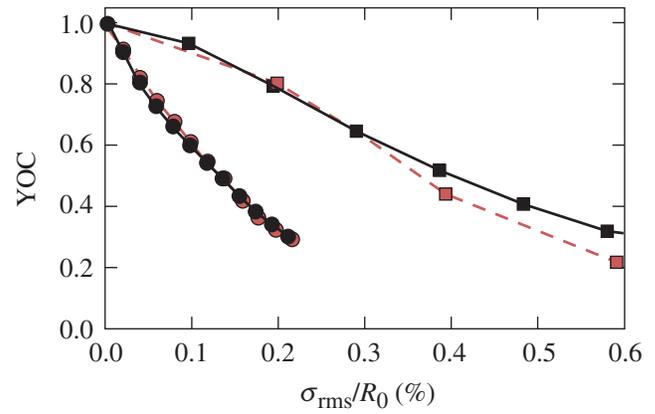
TC11081JR

Figure 137.9
Results from two-dimensional *DRACO* simulations plotting yield-over-clean (YOC) versus normalized ice roughness for NIF-scale (solid black lines) and OMEGA-scale (dashed red lines) targets for an ice spectrum with ℓ modes from 2 to 36 (squares) and 10 to 36 (circles).

Hydro-Equivalent Ignition Scaling of ICF Implosions

In this section, the hydrodynamic equivalence theory developed on p. 2 is applied to the Lawson criterion to create hydro-equivalent ignition-scaling relations for ICF implosions. A simple clean-volume analysis will be derived to estimate the scaling. Numerical simulations at the NIF and OMEGA scales are shown to support this result. Finally, ignition threshold performance metrics for hydro-equivalent ignition on OMEGA will be presented and discussed.

The Lawson criterion parameter defines the performance threshold required for an igniting plasma. It is defined as $\chi \equiv P\tau/P\tau_{ig}$, where P is the plasma pressure, τ is the confinement time, and $P\tau_{ig}$ is the product of the two required for ignition. The Lawson parameter can be expressed in terms of measurable parameters for ICF:[8,9]

$$\chi \equiv \left(\rho R_{g/cm^2}\right)^{0.61}\left(\frac{0.24\,Y_{16}}{m_{mg}^{DT}}\right)^{0.34}YOC^{0.06}, \qquad (35)$$

where $\rho R_{g/cm^2}$ is the 3-D neutron-averaged areal density in units of g/cm^2, Y_{16} is the 3-D neutron yield in units of 10^{16}, m_{mg}^{DT} is the mass of the DT fuel in milligrams, and YOC is the yield-over-clean defined as the measured yield over the simulated 1-D yield. All hydrodynamic quantities are calculated without alpha-particle deposition. The YOC is used as a measure of the impact of the 3-D nonuniformities such that $Y_{3\text{-}D} = Y_{1\text{-}D} \times YOC$. The YOC is also used to account for 3-D degradation of the areal density, where

$$\rho R_{3\text{-}D} \sim \rho R_{1\text{-}D} \times YOC^{0.17}. \qquad (36)$$

The power index of 0.17 is derived by fitting the areal-density degradation from several 2-D simulations as shown in Fig. 137.10. This stipulates the Lawson parameter to scale as $YOC^{0.5}$:

$$\chi = \left(\rho R_{g/cm^2}^{1\text{-}D}\right)^{0.61}\left(\frac{0.24\,Y_{16}^{1\text{-}D}}{m_{mg}^{DT}}\right)^{0.34}YOC^{0.5}. \qquad (37)$$

The Lawson parameter can be scaled from OMEGA to the NIF using the hydro-equivalence scaling laws derived in **Theory of Hyrodynamic Equivalence** (p. 2), where $\rho R_{1\text{-}D} \sim E^{1/3}$, $Y_{1\text{-}D} \sim E^{3/2}$, and $m \sim E$, to find

$$\chi \sim E^{0.37}YOC^{0.5}. \qquad (38)$$

Taking the ratio of Eq. (38) from two different implosions, we can compare one hydro-equivalent implosion to another in terms of the Lawson parameter. In this way it is possible to determine how close non-igniting implosions would be to achieving ignition if the laser energy and target geometry were hydro-equivalently scaled to an implosion that could ignite. Taking the definition of ignition to be when the implosion achieves marginal gain ($\chi = 1$), and assuming that ignition will occur at NIF's laser energy, the Lawson parameter for an OMEGA-scale implosion considered to be hydro-equivalently igniting would be

$$\chi_{\Omega-eq\,ig} = 0.21\left(\frac{YOC_{NIF}}{YOC_{\Omega}}\right)^{-0.5}. \qquad (39)$$

The YOC ratio in Eq. (39) is inferred using both an analytical clean volume analysis and 2-D hydrodynamic simulations.
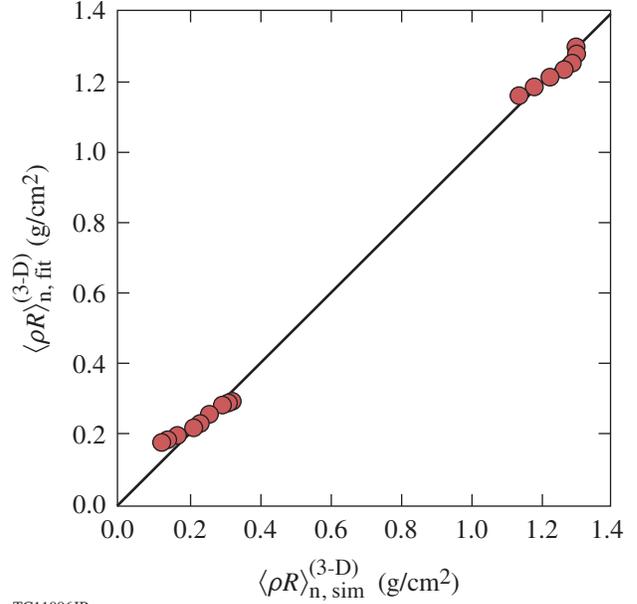
TC11096JR

Figure 137.10
Neutron-averaged 3-D areal density from simulations (red circles) compared to its numerical fit of Eq. (37) (solid black line).

A rough estimate of the YOC can be obtained by assuming that the YOC is proportional to the ratio of the clean volume to the 1-D volume: $YOC \approx R_{3\text{-}D}^3 \big/ R_{1\text{-}D}^3$ (Ref. 47). Using this approximation, it is possible to estimate the YOC ratio resulting from the RT growth in the deceleration phase. If we assume that the clean radius will decrease with the amplitude of the largest RT spike $R_{3\text{-}D} = R_{1\text{-}D} - \sigma_0 G_{RT}$, where σ_0 is the initial nonuniformity amplitude for the deceleration-phase RT and G_{RT} is the growth factor for RT modes, then a simple set of algebraic steps can relate the YOC's for the two hydro-equivalent implosions:

$$YOC_{NIF} = \left[1 - \frac{\sigma_0^{NIF}}{\sigma_0^{\Omega}}\left(\frac{E_L^{\Omega}}{E_L^{NIF}}\right)^{1/3}\left(1 - YOC_{\Omega}^{1/3}\right)\right]^3, \qquad (40)$$

where the growth factors are identical for the two hydro-equivalent implosions. Equation (40) recovers the results from the simulations shown in Fig. 137.9, where equal YOC's are obtained when using the same normalized σ_0. In most ICF implosions, however, laser-imprinting feedthrough will dominate the RT growth in the deceleration phase. It is possible to take this into account by setting $\sigma_0 \equiv \sqrt{\sigma_{ice}^2 + \sigma_{laser}^2}$, where σ_{laser} is the deceleration-phase nonuniformity seed amplitude resulting from laser imprinting. If the RT amplitude resulting from laser imprinting scales with the target size and the number of overlapping beams (N_b) such that $\sigma_{laser} \sim E^{1/3}N_b^{-1/2}$, then

$$\frac{\sigma_0^{\mathrm{NIF}}}{\sigma_0^{\Omega}} = \sqrt{\frac{1 + \left(E_{\mathrm{L}}^{\mathrm{NIF}} / E_{\mathrm{L}}^{\Omega}\right)^{2/3} \left(N_{\mathrm{b}}^{\Omega} / N_{\mathrm{b}}^{\mathrm{NIF}}\right)\hat{\sigma}_{\Omega}^{2}}{1 + \hat{\sigma}_{\Omega}^{2}}}, \qquad (41)$$

where $\hat{\sigma}_{\Omega} \equiv \sigma_{\mathrm{laser}} / \sigma_{\mathrm{ice}}$. Large values of $\hat{\sigma}_{\Omega}$ indicate that laser imprinting dominates the deceleration-phase nonuniformity seeds over the inner-ice-surface roughness. Inserting Eq. (41) into Eq. (40) and dividing by YOC_{Ω} gives an analytic expression for the YOC ratio and is shown in Fig. 137.11 for $N_{\mathrm{b}}^{\mathrm{NIF}} = 192$, $N_{\mathrm{b}}^{\Omega} = 60$, and $\mathrm{YOC}_{\Omega} = 0.3$. YOC_{Ω} is set to a value of 0.3 because this is a typical YOC experimentally inferred from the current best-performing cryogenic implosions on OMEGA.[42] This function asymptotes to a YOC ratio of 1.8 for large values of $\hat{\sigma}_{\Omega}$, representing the realistic regime where laser imprinting dominates over ice roughness. The YOC improvement of 1.8× is a result of the lower imprinting level in a NIF symmetric illumination configuration caused by the larger number of overlapping beams. Inserting this YOC ratio into Eq. (39) indicates that hydro-equivalent ignition would occur on an OMEGA-scale target obtaining $\chi_{\Omega-\mathrm{eq\ ig}} = 0.15$. It is important to emphasize that this conclusion is valid only within the simple YOC model shown above and assumes that the NIF imprinting level is lower than on OMEGA by a factor of $\sqrt{60/192}$.
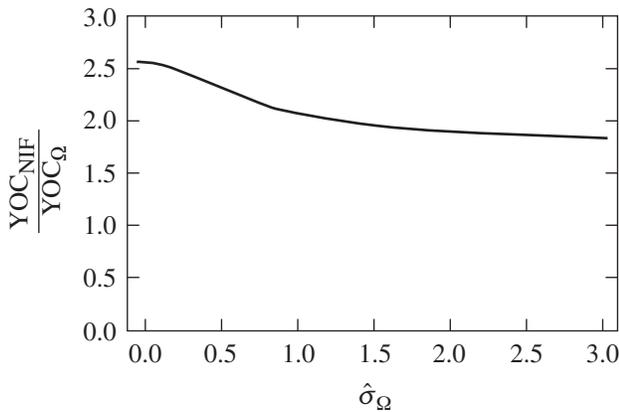
TC11082JR

Figure 137.11
Analytic calculation of the YOC ratio versus perturbation parameter $\hat{\sigma}_{\Omega}$ using a simple clean volume analysis. Large values of $\hat{\sigma}_{\Omega}$ are expected in experiments.

Two-dimensional multimode ice and imprinting simulations can be used to determine the YOC scaling ratio. These simulations have an imprint spectrum for a range of even ℓ modes from 2 to 100, a 1-μm root-mean-square ice roughness spectrum, and 2-D SSD laser-beam smoothing. Figure 137.12 plots the YOC of several simulations with varying degrees of laser
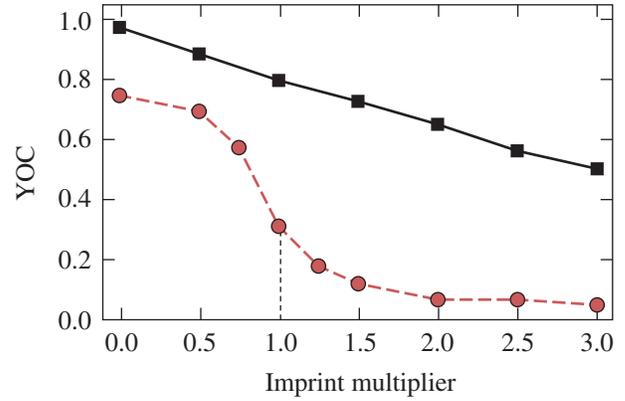
TC10877JR

Figure 137.12
Results from two-dimensional *DRACO* simulations plotting YOC versus an imprint multiplier for NIF-scale (solid black line) and OMEGA-scale (dashed red line) targets with expected inner-ice-surface roughness and variable laser imprinting. The vertical dashed line indicates a YOC_{Ω} of 0.30.

imprinting for both the NIF-scale and OMEGA-scale designs. The x axis is an amplitude multiplier on the imprint spectrum, where an imprint multiplier of zero indicates the simulation has perfectly smooth beams and an imprint multiplier of 1 indicates the expected level of imprint modulations being applied to the target for the 60-beam OMEGA or 192-beam symmetric NIF Laser Systems. The NIF-scale target with an imprint multiplier of zero has a YOC of 0.98, as a result of the relatively small effect of ice roughness, and decreases with increasing imprint multiplier. At an imprint multiplier of 2.67, the NIF-scale target achieves marginal ignition (gain = 1) when alpha-particle deposition is turned on. On the OMEGA-scale target, the reduction in YOC related to ice roughness only (~75%) is significantly larger than on the NIF-scale target. This is because the relative size of the ice roughness is larger by a factor of $\varepsilon^{1/3}$ on OMEGA with respect to the NIF, while the absolute magnitude of the ice roughness remains the same. The YOC of the OMEGA-scale target decreases as the imprint multiplier increases, albeit at a faster rate because the imprint spectrum is smoothed by a smaller number of beams. Above an imprint multiplier of 1, the OMEGA-scale target can be considered to be broken up. The OMEGA-scale line in Fig. 137.12 is an average of two sets of simulations where the phases of the ice roughness are reversed. Phase coupling's impact on target performance between the ice-roughness spectrum and the RT modes driven by laser imprinting can be significant and may lead to misinterpretation of the set of simulation results. For example, if the phases of the ice spectrum and laser imprinting destructively interfere, increasing the amount of laser imprinting can appear to have a positive effect on the YOC. Similarly, if the modes constructively interfere, the YOC reduction could

be grossly exaggerated. Averaging the YOC's from these two ice spectrums generalizes the impact of phase coupling and allows one to compare targets where phase coupling does not have a significant impact on target performance (such as the NIF-scale target).

The two curves in Fig. 137.12 contain all of the information necessary to infer the YOC ratio numerically. It is important to notice that the OMEGA-scale target exhibits a cliff in YOC when the imprint multiplier is above ~0.6. This occurs because the OMEGA-scale target begins to break up for such levels of nonuniformities, while the corresponding NIF target maintains its macroscopic integrity. Although the growth of hydrodynamic instabilities is essentially identical (i.e., hydro-equivalent) between the OMEGA-scale and NIF-scale targets, the seeds are not, resulting in very different behavior of the YOC as shown in Fig. 137.12. The difference in the relative level of nonuniformities between OMEGA-scale and NIF-scale targets breaks the hydro-equivalency. Even in the absence of laser imprinting, the relative size of the ice roughness is 4× larger on OMEGA than on the NIF. Therefore, both seeds of the RT instability (ice roughness and imprinting) are not hydro-equivalent. To achieve a final assessment of the performance requirements on OMEGA, we identify three possible extrapolations from OMEGA to the NIF:

1. A quasi-hydro-equivalent extrapolation corresponding to values of the YOC for OMEGA above 0.6 in Fig. 137.12. As shown in Fig. 137.12, in the range of YOC = 0.6 to 1.0, both the OMEGA and NIF targets remain integral during the implosion and are both above the shell's breakup "cliff." Full hydro-equivalency is not achieved because of the difference in relative ice roughness. The behavior of the YOC versus imprint multiplier is similar, however, even though the two curves are shifted and maintain an approximately constant ratio of 1.3. In this regime, extrapolations from OMEGA scales to NIF scales are likely to be quite reliable since the departure from hydro-equivalency is rather small (a factor of 1.3× in YOC and 1.05× in areal density).

2. A semi-hydro-equivalent extrapolation corresponding to values of the YOC for OMEGA between 0.3 and 0.6 in Fig. 137.12. The OMEGA shell is highly distorted and within the cliff in YOC. The OMEGA YOC is still reasonably high, however, and the clean hot-spot radius is larger than about 60% to 70% of its 1-D value. In this case, extrapolating from OMEGA scales to NIF scales requires a reliance on the hydrocode. This is not an

optimal or robust extrapolation since it relies on a large difference in calculated YOC's when extrapolating from OMEGA to the NIF.

3. A non-hydro-equivalent extrapolation corresponds to values of the YOC for OMEGA below 0.3 in Fig 137.12. The OMEGA shell is broken in flight and its performance is at the bottom of the YOC cliff, while the NIF target is still integral. The departure from hydro-equivalency is so great that it would be unreasonable to attempt an extrapolation from OMEGA experimental results to the NIF scale. We do not consider this regime viable for performance extrapolation.

We restrict our analysis to quasi- and semi-hydro-equivalent implosions [(1) and (2)] and limit the OMEGA-scale target YOC to values ≥0.3. Note that YOC's of 30% to 40% are the typical YOC's inferred from current high-performance implosions on OMEGA.[42] Figure 137.13 plots the YOC ratio versus YOC_Ω. It is observed that the YOC ratio varies from 1.3 to 2.7, depending on the level of laser imprinting. For smooth beams leading to a $YOC_\Omega \geq 0.6$ (quasi-hydro-equivalent regime), the YOC ratio is approximately 1.3—the predicted value given by the analytic scaling from Eq. (40) (for a YOC_Ω of 0.7). Larger imprinting levels increase the YOC ratio up to a factor of 2.7 at a YOC_Ω of 0.3 (semi-hydro-equivalent regime). It is important to note that the YOC ratio is not necessarily 2.7 but can range from 1.3 to 2.7, depending on the beam uniformity that is present on the NIF scale.
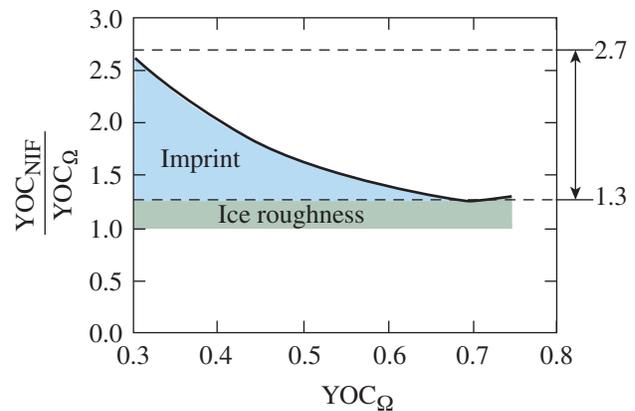
TC10878JR

Figure 137.13
YOC ratio determined from 2-D *DRACO* simulations as a function of YOC_Ω. A YOC ratio of 1.3 results from the impact of equal ice-roughness amplitudes, while a YOC ratio up to 2.7 resulting from laser imprinting is observed at YOC_Ω of 0.30.

The areal densities and neutron yields required for quasi- and semi-hydro-equivalent ignition on OMEGA follow from the 3-D Lawson criterion. Given the bounding values for the YOC ratio, $\chi_{\Omega-\text{eq ig}}$ can be calculated to be ~0.19 for quasi-hydro-equivalent ignition (YOC ratio of 1.3) and between 0.13 and 0.19 for semi-hydro-equivalent ignition (YOC ratio between 1.3 and 2.7). This indicates that any implosion occurring on OMEGA that obtains $\chi \geq \chi_{\Omega-\text{eq ig}}$ would equate to either quasi- or semi-hydro-equivalent ignition. Figure 137.14 is a contour plot of the 3-D Lawson criterion plotted against its two dependent variables—the 3-D neutron yield and the neutron-averaged areal density; the $YOC^{0.06}$ dependence is small enough to be ignored within a 10% error. For comparison, the white diamond indicates OMEGA's current best-performing shot in terms of the Lawson criterion ($\chi = 0.10$) (Ref. 42).
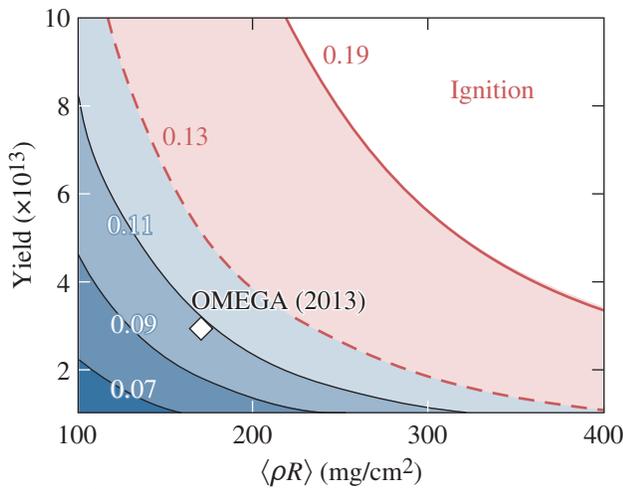
TC10879JR

Figure 137.14

Contour plot of the Lawson criterion parameter indicating the hydro-equivalent ignition threshold for OMEGA-scale targets (for YOC = 1). An OMEGA implosion lying within the white region indicates ignition would occur on a hydro-equivalent NIF-scale target. An implosion lying within the red region indicates potential hydro-equivalent ignition depending on the level of laser imprinting. An implosion lying within the blue region indicates ignition would not occur. The white diamond is the current best-performing implosion on OMEGA in terms of χ [note $\chi_\Omega = 0.10$ when taking into account the YOC term in Eq. (35)].

In summary, to claim quasi-hydro-equivalent ignition in a NIF symmetric illumination configuration, OMEGA's performance must increase from at least $\chi = 0.10$ to a minimum value of $\chi = 0.19$. To claim semi-hydro-equivalent ignition in a symmetric NIF illumination configuration, OMEGA's performance must increase from at least $\chi = 0.10$ to a minimum value of $\chi = 0.13$. It is important to emphasize that semi-hydro-

equivalent ignition for $\chi_{\Omega-\text{eq ig}} = 0.13$ uses a large enhancement (2.7×) in calculated yields from OMEGA to the NIF, thereby decreasing the reliability of such a conclusion. Table 137.II provides reasonable sample values required to demonstrate ignition on a quasi- and semi-hydro-equivalent symmetric NIF-scale target at the OMEGA scale in terms of neutron-averaged areal density and total neutron yield.

Table 137.II: Current OMEGA record performance metrics for experimentally measured neutron yields and neutron-averaged areal densities along with its calculated Lawson parameter χ. Sample values required to demonstrate hydro-equivalent ignition on OMEGA-scale cryogenic implosions are also provided.

	Neutron Yield ($\times 10^{13}$)	Areal Density (mg/cm^2)	$\chi_{\Omega-\text{eq ig}}$
OMEGA's current record (shot 69514)	3.0	173	0.10
Hydro-equivalent ignition (2.7 × YOC improvement)	3.0	240	0.13
Hydro-equivalent ignition (1.3 × YOC improvement)	6.0	300	0.19

Conclusions

Hydro-equivalence combined with ignition theory allows one to compare OMEGA-scale implosions to ignition-scale targets on a symmetric NIF illumination configuration with the same 2-D SSD smoothing as OMEGA. Hydro-equivalent implosions are energetically scalable and have identical implosion velocities, laser intensities, and adiabats. Hydro-equivalent implosions exhibit the same 1-D dynamics and the same hydro-dynamic instability growth. The measurable Lawson criterion was used to assess the performance of an implosion using experimental observables and can also be used in conjunction with hydro-equivalent scaling relations. Analytical derivations were developed and numerical simulations were performed to predict the hydro-equivalent ignition threshold on OMEGA-scale targets and are in good agreement with one another.

While OMEGA and NIF targets can be designed to be approximately hydro-equivalent, the difference in the initial level of nonuniformities prevents an exactly hydro-equivalent extrapolation. Ice roughness is inherently non-hydro-equivalent since the ice σ_{rms} is the same for OMEGA and the NIF while the OMEGA-scale's target size is roughly 4× smaller. Laser

imprinting is also non-hydro-equivalent because of the different number of beams between OMEGA and the NIF. In the absence of perfect hydro-equivalency, two OMEGA-to-NIF extrapolations have been identified: (a) a quasi-hydro-equivalent extrapolation including realistic ice roughness and relatively low levels of laser imprinting; (b) a semi-hydro-equivalent extrapolation applicable for a larger level of laser imprinting. A quasi-hydro-equivalent extrapolation requires OMEGA target performance characterized by YOC ≥ 0.6. The performance of such targets can be reliably extrapolated from OMEGA scale to the NIF scale since it requires a relatively small improvement in YOC of only 30%. A semi-hydro-equivalent extrapolation requires an OMEGA YOC of 0.3 to 0.6. The extrapolation to NIF scales from OMEGA-scale semi-hydro-equivalent implosions is less reliable since it requires a large calculated YOC improvement for ignition at NIF scales (up to 2.7× for an OMEGA YOC of 0.3).

In summary, the theory of hydro-equivalency and 2-D simulations of hydro-equivalent implosions indicates that a reliable extrapolation to ignition (quasi-hydro-equivalent ignition) on a symmetrically illuminating NIF configuration requires OMEGA target performance with an areal density of about 0.3 g/cm^2 and a neutron yield of about 6×10^{13}. As a short-term goal, semi-hydro-equivalent ignition on OMEGA requires less-demanding implosions that achieve areal densities and neutron yields as low as 0.24 g/cm^2 and 3×10^{13}, respectively.

ACKNOWLEDGMENT

REFERENCES

1. J. Nuckolls *et al.*, Nature **239**, 139 (1972).

2. S. E. Bodner, D. G. Colombant, J. H. Gardner, R. H. Lehmberg, S. P. Obenschain, L. Phillips, A. J. Schmitt, J. D. Sethian, R. L. McCrory, W. Seka, C. P. Verdon, J. P. Knauer, B. B. Afeyan, and H. T. Powell, Phys. Plasmas **5**, 1901 (1998).

3. J. D. Lindl, *Inertial Confinement Fusion: The Quest for Ignition and Energy Gain Using Indirect Drive* (Springer-Verlag, New York, 1998).

4. S. Atzeni and J. Meyer-ter-Vehn, *The Physics of Inertial Fusion: Beam Plasma Interaction, Hydrodynamics, Hot Dense Matter*, International Series of Monographs on Physics (Clarendon Press, Oxford, 2004).

5. O. A. Hurricane *et al.*, Nature **506**, 343 (2014).

6. J. D. Lawson, Proc. Phys. Soc. Lond. B **70**, 6 (1957).

7. J. P. Freidberg, *Plasma Physics and Fusion Energy* (Cambridge University Press, Cambridge, England, 2007).

8. R. Betti, P. Y. Chang, B. K. Spears, K. S. Anderson, J. Edwards, M. Fatenejad, J. D. Lindl, R. L. McCrory, R. Nora, and D. Shvarts, Phys. Plasmas **17**, 058102 (2010).

9. P. Y. Chang, R. Betti, B. K. Spears, K. S. Anderson, J. Edwards, M. Fatenejad, J. D. Lindl, R. L. McCrory, R. Nora, and D. Shvarts, Phys. Rev. Lett. **104**, 135002 (2010).

10. C. D. Zhou and R. Betti, Phys. Plasmas **15**, 102707 (2008).

11. B. K. Spears *et al.*, Phys. Plasmas **19**, 056316 (2012).

12. M. C. Herrmann, M. Tabak, and J. D. Lindl, Nucl. Fusion **41**, 99 (2001).

13. A. Kemp, J. Meyer-ter-Vehn, and S. Atzeni, Phys. Rev. Lett. **86**, 3336 (2001).

14. T. R. Boehly, D. L. Brown, R. S. Craxton, R. L. Keck, J. P. Knauer, J. H. Kelly, T. J. Kessler, S. A. Kumpan, S. J. Loucks, S. A. Letzring, F. J. Marshall, R. L. McCrory, S. F. B. Morse, W. Seka, J. M. Soures, and C. P. Verdon, Opt. Commun. **133**, 495 (1997).

15. S. Skupsky, R. W. Short, T. Kessler, R. S. Craxton, S. Letzring, and J. M. Soures, J. Appl. Phys. **66**, 3456 (1989).

16. J. D. Lindl, Phys. Plasmas **2**, 3933 (1995).

17. M. M. Basko, Nucl. Fusion **35**, 87 (1995).

18. W. M. Manheimer, D. G. Colombant, and J. H. Gardner, Phys. Fluids **25**, 1644 (1982).

19. R. D. Richtmyer, Commun. Pure. Appl. Math. **XIII**, 297 (1960).

20. E. E. Meshkov, Fluid Dyn. **4**, 101 (1969).

21. Lord Rayleigh, Proc. London Math Soc. **XIV**, 170 (1883).

22. G. Taylor, Proc. R. Soc. London Ser. A **201**, 192 (1950).

23. H. Takabe *et al.*, Phys. Fluids **28**, 3676 (1985).

24. R. Betti, V. N. Goncharov, R. L. McCrory, P. Sorotokin, and C. P. Verdon, Phys. Plasmas **3**, 2122 (1996).

25. D. L. Youngs, Physica **12D**, 32 (1984).

26. D. Oron, U. Alon, and D. Shvarts, Phys. Plasmas **5**, 1467 (1998).

27. S. W. Haan, Phys. Fluids B **3**, 2349 (1991).

28. S. W. Haan, Phys. Rev. A **39**, 5812 (1989).

29. V. Lobatchev and R. Betti, Phys. Rev. Lett. **85**, 4522 (2000).

30. L. Spitzer, *Physics of Fully Ionized Gases* (Interscience Publishers, New York, 1956).

31. C. D. Zhou and R. Betti, Phys. Plasmas **14**, 072703 (2007).

32. J. F. Myatt, J. Zhang, R. W. Short, A. V. Maximov, W. Seka, D. H. Froula, D. H. Edgell, D. Michel, I. V. Igumenshchev, D. E. Hinkel, and P. Michel, "Multibeam Laser–Plasma Interactions in Inertial Confinement Fusion," to be published in Physics of Plasmas.

33. I. V. Igumenshchev, D. H. Edgell, V. N. Goncharov, J. A. Delettrez, A. V. Maximov, J. F. Myatt, W. Seka, A. Shvydky, S. Skupsky, and C. Stoeckl, Phys. Plasmas **17**, 122708 (2010).

34. I. V. Igumenshchev, W. Seka, D. H. Edgell, D. T. Michel, D. H. Froula, V. N. Goncharov, R. S. Craxton, L. Divol, R. Epstein, R. Follett, J. H. Kelly, T. Z. Kosc, A. V. Maximov, R. L. McCrory, D. D. Meyerhofer, P. Michel, J. F. Myatt, T. C. Sangster, A. Shvydky, S. Skupsky, and C. Stoeckl, Phys. Plasmas **19**, 056314 (2012).

35. D. H. Froula, I. V. Igumenshchev, D. T. Michel, D. H. Edgell, R. Follett, V. Yu. Glebov, V. N. Goncharov, J. Kwiatkowski, F. J. Marshall, P. B. Radha, W. Seka, C. Sorce, S. Stagnitto, C. Stoeckl, and T. C. Sangster, Phys. Rev. Lett. **108**, 125003 (2012).

36. D. H. Edgell, W. Seka, J. A. Delettrez, R. S. Craxton, V. N. Goncharov, I. V. Igumenshchev, J. F. Myatt, A. V. Maximov, R. W. Short, T. C. Sangster, and R. E. Bahr, Bull. Am. Phys. Soc. **54**, 145 (2009).

37. W. Seka, D. H. Edgell, J. F. Myatt, A. V. Maximov, R. W. Short, V. N. Goncharov, and H. A. Baldis, Phys. Plasmas **16**, 052701 (2009).

38. R. W. Short, Bull. Am. Phys. Soc. **53**, 245 (2008).

39. D. T. Michel, A. V. Maximov, R. W. Short, S. X. Hu, J. F. Myatt, W. Seka, A. A. Solodov, B. Yaakobi, and D. H. Froula, Phys. Rev. Lett. **109**, 155007 (2012).

40. J. F. Myatt, J. Zhang, J. A. Delettrez, A. V. Maximov, R. W. Short, W. Seka, D. H. Edgell, D. F. DuBois, D. A. Russell, and H. X. Vu, Phys. Plasmas **19**, 022707 (2012).

41. D. T. Michel, A. V. Maximov, R. W. Short, J. A. Delettrez, D. Edgell, S. X. Hu, I. V. Igumenshchev, J. F. Myatt, A. A. Solodov, C. Stoeckl, B. Yaakobi, and D. H. Froula, Phys. Plasmas **20**, 055703 (2013).

42. T. C. Sangster, V. N. Goncharov, R. Betti, P. B. Radha, T. R. Boehly, D. T. Casey, T. J. B. Collins, R. S. Craxton, J. A. Delettrez, D. H. Edgell, R. Epstein, C. J. Forrest, J. A. Frenje, D. H. Froula, M. Gatu-Johnson, V. Yu. Glebov, D. R. Harding, M. Hohenberger, S. X. Hu, I. V. Igumenshchev, R. Janezic, J. H. Kelly, T. J. Kessler, C. Kingsley, T. Z. Kosc, J. P. Knauer, S. J. Loucks, J. A. Marozas, F. J. Marshall, A. V. Maximov, R. L. McCrory, P. W. McKenty, D. D. Meyerhofer, D. T. Michel, J. F. Myatt, R. D. Petrasso, S. P. Regan, W. Seka, W. T. Shmayda, R. W. Short, A. Shvydky, S. Skupsky, J. M. Soures, C. Stoeckl, W. Theobald, V. Versteeg, B. Yaakobi, and J. D. Zuegel, Phys. Plasmas **20**, 056317 (2013).

43. P. B. Radha, V. N. Goncharov, T. J. B. Collins, J. A. Delettrez, Y. Elbaz, V. Yu. Glebov, R. L. Keck, D. E. Keller, J. P. Knauer, J. A. Marozas, F. J. Marshall, P. W. McKenty, D. D. Meyerhofer, S. P. Regan, T. C. Sangster, D. Shvarts, S. Skupsky, Y. Srebro, R. P. J. Town, and C. Stoeckl, Phys. Plasmas **12**, 032702 (2005).

44. G. I. Kerley, Phys. Earth Planet. Inter. **6**, 78 (1972).

45. G. I. Kerley, Sandia National Laboratory, Albuquerque, NM, Report SAND2003-3613 (2003).

46. S. X. Hu, B. Militzer, V. N. Goncharov, and S. Skupsky, Phys. Rev. B **84**, 224109 (2011).

47. R. Kishony and D. Shvarts, Phys. Plasmas **8**, 4925 (2001).